



Light localization and SERS in tip-shaped silicon metasurface

ANDREY LAGARKOV,¹ IRINA BOGINSKAYA,¹ IGOR BYKOV,¹ IGOR BUDASHOV,² ANDREY IVANOV,¹ ILYA KUROCHKIN,^{2,3} ILYA RYZHIKOV,^{1,4,5} ILYA RODIONOV,^{4,5} MARINA SEDOVA,¹ ALEXANDER ZVEREV,^{4,5} AND ANDREY K. SARYCHEV^{1,*}

¹*Institute for Theoretical and Applied Electrodynamics, Russian Academy of Sciences, Russia*

²*Faculty of Chemistry, Moscow State University, Russia*

³*Emanuel Institute of Biochemical Physics, Russian Academy of Sciences, Moscow, Russia*

⁴*All-Russia Research Institute of Automatics, Moscow, Russia*

⁵*Bauman Moscow State Technical University, Russia*

**sarychev_andrey@yahoo.com*

Abstract: Optical properties of two dimensional periodic system of the silicon micro-cones are investigated. The metasurface, composed of the silicon tips, shows enhancement of the local optical field. Finite element computer simulations as well as real experiment reveal anomalous optical response of the dielectric metasurface due to excitation of the dielectric resonances. Various electromagnetic resonances are considered in the dielectric cone. The metal-dielectric resonances, which are excited between metal nanoparticles and dielectric cones, are also considered. The resonance local electric field can be much larger than the field in the usual surface plasmon resonances. To investigate local electric field the signal molecules are deposited on the metal nanoparticles. We demonstrate enhancement of the electromagnetic field and Raman signal from the complex of *DTNB* acid molecules and gold nanoparticles, which are distributed over the metasurface. The metasurfaces composed from the dielectric resonators can have quasi-continuous spectrum and serve as an efficient SERS substrates.

© 2017 Optical Society of America

OCIS codes: (260.0260) Physical optics; (240.0240) Optics at surfaces; (240.6695) Surface enhanced Raman Scattering.

References and links

1. K. J. Vahala, "Optical microcavities," *Nature* **424**, 839–846 (2003).
2. T. Aoki, B. Dayan, E. Wilcut, W. Bowen, A. Parkins, T. Kippenberg, K. Vahala, and Imble, "Observation of strong coupling between one atom and a monolithic micro-resonator," *Nature* **443**, 671–674 (2006).
3. B. Min, E. Ostby, V. Sorger, E. Ulin-Avila, L. Yang, X. Zhang, and K. Vahala, "High-Q surface-plasmon-polariton whispering-gallery microcavity," *Nature* **457**, 455–458 (2009).
4. H. Tureci, H. Schwefe, P. Jacquod, and D. Stone, "Modes of wave-chaotic dielectric resonators," *Progress in Optics* **47**, 75–108 (2005).
5. L. Rayleigh, "The problem of whispering gallery," *Phil. Mag.* **20**, 1001–1004 (1904).
6. D. K. Armani, T. J. Kippenberg, S. M. Spillane, and K. J. Vahala, "Ultra-high-Q toroid microcavity on a chip," *Nature* **421**, 925–928 (2003).
7. T. Herr, V. Brasch, J. D. Jost, I. Mirgorodskiy, G. Lihachev, M. L. Gorodetsky, and T. J. Kippenberg, "Mode spectrum and temporal soliton formation in optical microresonators," *Phys. Rev. Lett.* **113**, 123901–5 (2014).
8. A. A. Savchenkov, A. B. Matsko, V. S. Ilchenko, and L. Maleki, "Optical resonators with ten million nesses," *Opt. Express* **15**, 6768–6773 (2007).
9. Y. Dumeige, S. Trebaol, L. Ghisa, T. K. N. Nguyen, H. Tavernier, and P. Feron, "Determination of coupling regime of high-Q resonators and optical gain of highly selective amplifiers," *J. Opt. Soc. Am. B* **25**, 2073–2080 (2007).
10. A. C. Tamboli, E. D. Haberer, R. Sharma, K. H. Lee, S. Nakamura, and E. L. Hu, "Room-temperature continuous-wave lasing in GaN/InGaN microdisks," *Nat. photonics* **1**, 61–64 (2007).
11. M. L. Gorodetsky, A. A. Savchenkov, and V. S. Ilchenko, "Ultimate Q of optical microsphere," *Opt. Lett.* **21**, 453–455 (1996).
12. M. Sumetsky, "Mode localization and the Q-factor of a cylindrical microresonator," *Opt. Lett.* **35**, 2385–2387 (2010).
13. M. Sumetsky, "Whispering-gallery-bottle microcavities: the three-dimensional etalon," *Opt. Lett.* **29**, 8–10 (2004).
14. M. Sumetsky, "Localization of light on a cone: theoretical evidence and experimental demonstration for an optical fiber," *Opt. Lett.* **29**, 145–147 (2011).

15. A. A. Barannik, S. A. Bunyaev, and N. T. Cherpak, "Conical quasioptical dielectric resonator," *Tech. Phys. Lett.* **31**, 811–812 (2005).
16. A. A. Kishk, Y. Yin, and A. W. Glisson, "Conical dielectric resonator antennas for wide-band applications," *IEEE Trans. Antennas Propag.* **50**, 469–474 (2002).
17. F. Vollmer and S. Arnold, "Whispering-gallery-mode biosensing: label-free detection down to single molecules," *Nat. Methods* **5**, 591–596 (2008).
18. V. R. Dantham, S. Holler, V. Kolchenko, Z. Wan, and S. Arnold, "Taking whispering gallery-mode single virus detection and sizing to the limit," *Appl. Phys. Lett.* **101**, 043704 (2012).
19. H. Cao and J. Wiersig, "Dielectric microcavities: Model systems for wave chaos and non-Hermitian physics," *Rev. Mod. Phys.* **87**, 61–111 (2015).
20. C. Gmachl, F. Capasso, E. E. Narimanov, J. U. Nöckel, A. Douglas Stone, J. Faist, D. L. Sivco, and A. Y. Cho, "High-power directional emission from microlasers with chaotic resonators," *Science* **280**, 1556–1564 (1998).
21. W. Fang, H. Cao, V. A. Podolskiy, and E. E. Narimanov, "Dynamical localization in microdisk lasers," *Opt. Express* **13**, 5641–5652 (1998).
22. C. Claire, E. E. Narimanov, F. Capasso, J. N. Baillargeon, and A. Y. Cho, "Kolmogorov-Arnold-Moser transition and laser action on scar modes in semiconductor diode lasers with deformed resonators," *Opt. Lett.* **27**, 824–826 (2002).
23. A. Lagarkov, I. Budashov, V. Chistyayev, A. Ezhov, A. Fedyanin, A. Ivanov, I. Kurochkin, S. Kosolobov, A. Latyshev, D. Nasmimov, I. Ryzhikov, M. Shcherbakov, A. Vaskin, and A. K. Sarychev, "SERS-active dielectric metamaterials based on periodic nanostructured," *Opt. Express* **24**, 7133–7150 (2016).
24. S. S. Vergeles, A. K. Sarychev, and G. Tartakovskiy, "All-dielectric light concentrator to subwavelength volume," *Phys. Rev. B* **95**, 085401 (2017).
25. B. Yan, A. Thubagere, W. R. Premasiri, L. D. Ziegler, L. D. Negro, B. M. Reinhard, "Engineered SERS substrates with multiscale signal enhancement: nanoparticle cluster arrays," *ACS Nano* **3**, 1190–1202 (2009).
26. F. Brouers, S. Blacher, A. N. Lagarkov, A. K. Sarychev, P. Gadenne, and V. M. Shalaev, "Theory of Giant Raman Scattering from Semicontinuous Metal Films," *Phys. Rev. B* **55**, 13234–13245 (1997).
27. A. K. Sarychev and V. M. Shalaev, *Electrodynamics of Metamaterials*, (World Scientific, 2007).
28. S. O. Boyarintsev and A. K. Sarychev, "Computer Simulation of Surface-Enhanced Raman Scattering in Nanostructured Metamaterials," *JETP* **113**, 1103–1110 (2011).
29. A. V. Ivanov, A. V. Vaskin, A. N. Lagarkov, and A. K. Sarychev, "The field enhancement and optical sensing in the array of almost adjoining metal and dielectric nanorods," *Proc. SPIE* **9163**, 91633C1–C13 (2014).
30. M. Cottat, N. Lidgi-Guigui, I. Tijunelyte, G. Barbillon, F. Hamouda, P. Gogol, A. Aassime, J.-M. Lourtioz, B. Bartenlian, and M. L. de la Chapelle, "Soft UV nanoimprint lithography-designed highly sensitive substrates for SERS detection," *Nanoscale Res. Lett.* **9**, 623 (2014).
31. I. S. Kurochkin, I. A. Ryzhikov, A. K. Sarychev, K. N. Afanasiev, I. A. Budashov, M. S. Sedova, I. A. Boginskaya, S. Amitonov, and A. N. Lagarkov, "New SERS-active junction based on cerium dioxide facet dielectric films for biosensing," *Adv. Electromagn.* **3**, 57 (2014).
32. A. Delfan, M. Liscidini, and J. E. Sipe, "Surface enhanced Raman scattering in the presence of multilayer dielectric structures," *J. Opt. Soc. Am. B* **29**, 1863–1874 (2012).
33. A. I. Kuznetsov, A. E. Miroshnichenko, Y. H. Fu, J. Zhang, and B. Luk'yanchuk, "Magnetic light," *Sci. Rep.* **2**, 492–497 (2012).
34. P. Albella, M. A. Poyli, M. K. Schmidt, S. A. Maier, F. Moreno, J. J. Saenz, J. Aizpurua, "Low-Loss Electric and Magnetic Field-Enhanced Spectroscopy with Subwavelength Silicon Dimers," *J. Phys. Chem. C* **117**, 13573–13584 (2013).
35. R. M. Bakker, D. Permyakov, Y. F. Yu, D. Markovich, R. Paniagua-Dominguez, L. Gonzaga, A. Samusev, Y. Kivshar, B. Luk'yanchuk, and A. I. Kuznetsov, "Magnetic and Electric Hotspots with Silicon Nanodimers," *Nano Lett.* **15**, 2137–2142 (2015).
36. A. E. Krasnok, A. E. Miroshnichenko, P. A. Belov, and Y. S. Kivshar, "All-dielectric optical nanoantennas," *Opt. Express* **20**, 20599–20604 (2012).
37. Y. Hong, M. Pourmand, S. V. Boriskina, and B. M. Reinhard, "Enhanced light focusing in self-assembled optoplasmonic clusters with subwavelength dimensions," *Adv. Mater.* **25**, 115–119 (2013).
38. Y. Hong, Y. Qiu, T. Chen, and B. M. Reinhard, "Rational assembly of optoplasmonic hetero-nanoparticle arrays with tunable photonic-plasmonic resonances," *Adv. Funct. Mater.* **24**, 739–746 (2014).
39. S. Jahani and Z. Jacob, "All-dielectric metamaterials," *Nat. Nanotechnol.* **11**, 23–36 (2016).
40. S. Jahani and Z. Jacob, "Transparent subdiffraction optics: nanoscale light confinement without metal," *Optica* **1**, 96–100 (2014).
41. J. Zhang, W. Liu, Z. Zhu, X. Yuan, and S. Qin, "Strong field enhancement and light-matter interactions with all-dielectric metamaterials based on split bar resonators," *Opt. Express* **22**, 30889–30898 (2014).
42. A. V. Maslov, V. N. Astratov, "Imaging of sub-wavelength structures radiating coherently near microspheres," *Appl. Phys. Lett.* **108**, 051104 (2016).
43. A. S. Shorokhov, E. V. Melik - Gaykazyan, D. A. Smirnova, B. Hopkins, K. E. Chong, D.-Y. Choi, M. R. Shcherbakov, A. E. Miroshnichenko, D. N. Neshev, A. A. Fedyanin, and Y. S. Kivshar, "Multifold enhancement of third-harmonic generation in dielectric nanoparticles driven by magnetic Fano resonances," *Nano Lett.* **16**, 4857–4861 (2016).
44. S. J. Kim, P. Fan, J.-H. Kang, and M. L. Brongersma, "Creating semiconductor metafilms with designer absorption

- spectra,” *Nature Communications* **6**, 7591–7595 (2015).
45. A. V. Ivanov, A. S. Vaskin, A. N. Lagarkov, and A. K. Sarychev, “The field enhancement and optical sensing in the array of almost adjoining metal and dielectric nanorods,” *Proc. SPIE* **9163**, 91633C1–91633C13 (2014).
 46. K. Afanasiev, I. Boginskaya, I. Budashov, A. Ivanov, I. Kurochkin, A. Lagarkov, I. Ryzhikov, and A. Sarychev, “Giant field fluctuations in dielectric metamaterials and Raman sensors,” *Proc. SPIE*, **9544**, 95441Y1 (2015).
 47. A. Lagarkov, I. Kurochkin, I. Ryzhikov, A. Vaskin, K. Afanasiev, I. Boginskaya, I. Budashov, and A. Sarychev, “Surface dielectric resonance and giant enhancement of Raman scattering,” *Proc. SPIE*, **9161**, 91610 (2014).
 48. H. Xu, E. J. Bjerneld, M. Kall, and L. Borjesson, “Spectroscopy of single hemoglobin molecules by Surface Enhanced Raman Scattering,” *Phys. Rev. Lett.* **83**, 4357–4360 (1999).
 49. I. N. Kurochkin, A. K. Sarychev, I. A. Ryzhikov, I. A. Budashov, S. S. Maklakov, S. O. Boyarintsev, and A. N. Lagarkov, “Surface-enhanced raman scattering based biosensors,” in *Portable biosensing of food toxicants and environmental pollutants*, D. P. Nikolelis, T. Varzakas, A. Erdem, and G.-P. Nikoleli, eds. (CRC Press, 2014), pp. 97–122.
 50. M. S. Kiran, T. Itoh, K. Yoshida, N. Kawashima, V. Biju, and M. Ishikawa, “Selective detection of HbA1c using surface enhanced resonance Raman spectroscopy,” *Anal. Chem.* **82**, 1342–1348 (2010).
 51. M. A. Green and M. J. Keevers, “Optical properties of intrinsic silicon at 300 K,” *Prog. Photovoltaics* **9163**, 189–192 (1995).
 52. A. Garcia-Etxarri, R. Gomez-Medina, L. S. Froufe-Perez, C. Lopez, L. Chantada, F. Scheffold, J. Aizpurua, M. Nieto-Vesperinas, and J. J. Saenz, “Strong magnetic response of submicron silicon particles in the infrared,” *Opt. Express* **19**, 4815–4826 (2011).
 53. C. E. Soteropulos, H. K. Hunt, and A. M. Armani, “Determination of binding kinetics using whispering gallery mode microcavities,” *Appl. Phys. Lett.* **99**, 103703–3 (2011).
 54. S. I. Shopova, R. Rajmangal, S. Holler, and S. Arnold, “Plasmonic enhancement of a whispering-gallery-mode biosensor for single nanoparticle detection,” *Appl. Phys. Lett.* **98**, 243104–3 (2011).
 55. A. Armani, R. Kulkarni, S. Fraser, R. Flagan, and K. Vahala, “Label-free, single-molecule detection with optical microcavities,” *Science* **317**, 783–787 (2007).
 56. Y. Brule, G. Demesy, B. Gralak, and E. Popov, “Surface plasmon hurdles leading to a strongly localized giant field enhancement on two-dimensional (2D) metallic diffraction gratings,” *Opt. Express* **23**, 9167–9182 (2015).
 57. K. Li, M. I. Stockman, and D. J. Bergman, “Self-similar chain of metal nanospheres as an efficient nanolens,” *Phys. Rev. Lett.* **91**, 227402-4 (2003).
 58. D. A. Schultz, “Plasmon resonant particles for biological detection,” *Curr. Opin. Biotech.* **14**, 13–22 (2003).
 59. A. Ivanov, A. Shalygin, V. Lebedev, P. Vorobev, S. Vergiles, and A.K. Sarychev, “Plasmonic extraordinary transmittance in array of metal nanorods,” *Appl. Phys. A* **107**, 17–21 (2012).
 60. P. B. Johnson and R. W. Christy, “Optical constants of the noble metals,” *Phys. Rev. B.* **6**, 4370–4379 (1972).
 61. A. Kristensen, J. K. W. Yang, S. I. Bozhevolnyi, S. Link, P. Nordlander, N. J. Halas, and N. A. Mortensen “Plasmonic colour generation,” *Nat. Rev. Mat.* **2**, 16088 (2016).
 62. E. Prodan, C. Radloff, N.J. Halas, and P. A. Nordlander, “Hybridization model for the plasmon response of complex nanostructures,” *Science* **302**, 419 - 422 (2003).
 63. Y. Hong and B. M. Reinhard, “Collective photonic-plasmonic resonances in noble metal-dielectric nanoparticle hybrid arrays,” *Opt. Mat. Express* **4**, 2409–2422 (2014).
 64. S. Pi, X. Zeng, N. Zhang, D. Ji, B. Chen, H. Song, A. Cheney, Y. Xu, S. Jiang, S. Sun, Y. Song, and Q. Gan, “Dielectric-grating-coupled surface plasmon resonance from the back side of the metal film for ultrasensitive sensing,” *IEEE Photonics J.* **8**, 4800207 (2016).
 65. M. A. Santiago-Cordoba, S. V. Boriskina, F. Vollmer, and M. C. Demirel, “Nanoparticle-based protein detection by optical shift of a resonant microcavity,” *Appl. Phys. Lett.* **99**, 073701 (2011).
 66. J. Turkevich, P. S. Stevenson, and J. Hiller, “A study of the nucleation and growth processes in the synthesis of colloidal gold,” *Discuss. Faraday Soc.* **11**, 55–75 (1955).
 67. M. G. Gromova, L. V. Sigolaeva, M. A. Fastovets, E. G. Evtushenko, I. A. Babin, D. V. Pergushov, S. A. Amitonov, A. V. Eremenko, and I. N. Kurochkin, “Improved absorption of choline oxidase on a polyelectrolyte LBL film in the presence of iodine anions,” *Soft Matter*. **7**, 7404–7409 (2011).

1. Introduction

The low-loss and high quality optical dielectric resonators attract much attention due to the importance for the fundamental and applied research. Optical microcavities can greatly enhance light-matter interactions by storing optical energy in small volumes. The ability to concentrate light is important not only to fundamental physics studies, but also for R&D of many new hi-tech devices. Optical microcavities confine light to small volumes by resonant recirculation. Devices based on the optical microcavities are already indispensable for a wide range of applications and studies. For example, microcavities made of active III-V semiconductor materials control laser emission spectra to enable long-distance transmission of data over optical fibers; they also ensure

narrow spot-size laser read/write beams in CD and DVD players. In quantum optical devices, microcavities can force the atoms or quantum dots to emit spontaneous photons in a desired direction or can provide an environment, where dissipative mechanisms such as spontaneous emission are overcome so that quantum entanglement of the radiation and matter is possible (see, e.g., [1–3]).

Electromagnetic resonances can be excited in any piece of a low loss dielectric. Yet, quality factor Q is very different for various em modes so that some of them are very lossy even in a rather large resonator [4]. Among all em modes the whispering-gallery modes (WGM) have large quality Q . Some interactions of light with dielectric interfaces could be associated with the phenomenon of WGM, which is known for hundreds years [5]. The effect of the "Whispering galleria" comes from architectural acoustics when the sound propagates not along the shortest path, but rather along the concave surfaces. It is well known that the light can suffer the total internal reflection at the boundary while it propagates from the denser medium to the less dense medium at the small angle of incidence. Therefore, whispering gallery waves can be explained as the waves of the total internal reflection. Typically WGM resonators are made of silica, CaF_2 , MgF_2 , GaN , $GaAs$ etc. WGM resonators typically have shape of disk, sphere, cylinder, or torus. The quality factor Q in a WGM resonators can be as large as 10^7 and 10^9 [6–12].

Most of work that has been done so far is done on the disk or spherical resonators. More complicated three-dimensional resonators have additional degrees of freedom and can produce interesting effects that do not exist in a simple geometry. Thus, localization of light in bottle-shaped resonator with varying radius, that called "whispering gallery bottle" was proposed in work [13]. The conical dielectric resonators were studied in [14–16]. In work [14] it was shown that small variation of an optical microcylinder radius results in strongly localized conical WGMs.

Because of extraordinary high Q-factor, WGM resonators can be used in optical devices such as filters, modulators, switches, sensors, lasers, et al. The extremely long lifetime in a WGM makes it sensitive to absorption of a single molecule or virus onto the cavity surface [17, 18]. The phenomena of quantum chaos in WGM resonators is reported in works [19–22]. It was shown that depending on the type and degree of shape deformation of the circular boundary, whispering gallery orbits can evolve from regular to fully or partially chaotic.

Since the resonances in dielectric and combined metal-dielectric nano and microstructures lead to the focusing of giant local electromagnetic fields, it can be used for the surface enhanced Raman scattering (SERS), see for example, [23–32]. The electric and magnetic fields concentration in the dielectric micro-structures attracts a lot of attention in recent years [19, 33]. The electric field enhancement between two neighboring resonating dielectric spheres was predicted [34] and observed in the experiment [35] for the nanodimer consisting of two silicon nanocylinders of diameter 140, height 150, and gap 30 nm. The chain of six dielectric nanoparticles was suggested as Yagi-Uda antenna [36]. The dielectric Yagi-Uda antenna much increases the radiation of a dipole placed between first and second particles. It is clear that the antenna will concentrate the incident light in the same point. Enhanced light focusing was proposed and observed in the work [37], where the authors investigate a ring of plasmonic metal nanoparticles interacting with each other and with adjoining dielectric micro resonator. The plasmon resonance in the plasmonic ring results in a considerable increase of the em field near the surface of the dielectric micro resonator far away from the ring. Note that the electric field is much less enhanced in the case of spatially separated metal clusters and dielectric micro resonators [38]. The light propagation in dielectric metamaterials is discussed in the review [39]. For example, the em wave can be much confined within sub-wavelength scale in the dielectric waveguide with anisotropic cladding [40]. The electric field concentration due to a resonance between periodic dielectric rectangular resonators was simulated [41], super resolution of the resonate microstructures can be achieved by a dielectric microsphere (see [42] and references therein). The enhancement of optical nonlinearity was observed [43] due to the magnetic resonance in the system of four

closely packed dielectric disks. Effective absorption of em energy in the periodic semiconductor metafilms was investigated for the solar cells (see [44] and reference therein). A strong electric field enhancement and SERS in periodic metafilms, constructed from the dielectric micro beams were obtained in [23, 45] for microwave and optical spectral ranges. Distributed dielectric resonances in randomly faceted ceria metafilms were also considered [31, 46, 47]. Dielectric metamaterials can be used for the bio-sensing [48–50].

In our work we investigate the light interaction with tip-shaped, regular dielectric metasurface made of the silicon cones. Cone shaped tips exhibit various dielectric resonances in visible and near IR spectral ranges. We develop the analytical theory of both electric and magnetic resonances in the sub-wavelength high refraction conical resonator and obtain a spectrum of resonances. The tip-shaped metasurface reveals an anomalous bright diffraction in the visible spectrum range. We also investigate metal-dielectric resonances, where an anomalous large em field can be achieved. Gold nanoparticles are placed on the surface of silicon micro tips. We discuss in details the structure of the metal-dielectric resonance. Computer simulations are performed for plasmon resonances in single or dimer gold nanoparticles placed on the tip surface. We use a system of tip-shaped silicon surface with immobilized gold nanoparticles to demonstrate SERS phenomenon. DTNB (5, 5'-dithio-bis-[2-nitrobenzoic acid]) molecules are immobilized on the surface of gold nanoparticles. A semicontinuous molecular mono-layer is used as an effective indicator of the local field enhancement and SERS phenomenon.

2. Anomalous diffraction by tip-shaped metasurface

We investigate an optical metasurface. The experimental samples are fabricated by NT-MDT Inc., Moscow. The dielectric metasurface is made of silicon cone-shaped grating as it is shown in Fig. 1(a). The geometric parameters are: square lattice with the period $d = 2.1 \mu\text{m}$, height $0.3 - 0.7 \mu\text{m}$, the cone opening angle $2\theta_0 \approx 30^\circ$ degrees, the tip curvature radius $\leq 10 \text{ nm}$, the whole area $2 \times 2 \text{ mm}$. The metasurface can be considered as a diffraction grating since the inter-particle spacing d is larger than the wavelength λ in the visible spectral range. It is well known that the condition for the positive interference is that the difference in optical paths equals to an integer number of the vacuum wavelengths. The existence of a higher diffraction order requires that $-1 < m_1\lambda/d < 1$, $-1 < m_2\lambda/d < 1$, where m_1 and m_2 are diffraction orders. For example, in the case for the red laser $\lambda = 632.8 \text{ nm}$ (see Figs. 2 and 3), there are 37 diffracting modes: the mode with $m_1 = m_2 = 0$ is the reflected wave, whereas orders with $m_1 = m_2 = \pm 1, 2, 3$ are the diffracted waves.

In our experiment we use a traditional approach. The red laser beam ($\lambda = 632.8 \text{ nm}$), directed through the circular hole in the screen, reflects from the metasurface. The micro-tip diffraction produces a pattern on the backside of the screen, as it is shown Fig. 2. The parameters are: laser power $I = 34.8 \text{ mW}$, the circular hole diameter 1.0 mm , the distance between the screen and the metasurface is 20 mm . The sample was rotated with respect to the point of zero diffraction order by 0.5° degrees to exclude the spurious reflectance.

The diffraction pattern reveals all 37 modes which have different radiance $I(m_1, m_2)$ as it is shown in Fig. 3(a). The total reflection $R = R_{00} + \sum R_{m_1 m_2}$ is estimated as ≈ 0.32 , where 0.26 corresponds to zero order reflectance and 0.06 - to the diffraction. In other words, 19% of the reflected energy goes to the diffraction beams. The silicon tips cover only 8% of the total area of the metasurface. Hence they provide a very effective diffraction, which could be called an "extraordinary" optical diffraction. A similar experiment for the blue laser beam with $\lambda = 405 \text{ nm}$ also gives a bright diffraction pattern [Fig. 3(b)], in spite of a large optical loss in silicon for wavelengths ($\lambda < 500 \text{ nm}$) (see, e.g., [51]). It is not surprising since the electric field is greatly enhanced on the surface of a sharp tip regardless of the loss as it is discussed below in Sec. 3

The diffraction pattern does not change when we shift the system with respect to the laser spot. Therefore, it is safe to suppose that periodicity and cone shape are well defined all over the

metasurface. In the next section we consider the electric field enhancement due to em resonances in a silicone cone. The maximum enhancement comes from the resonance between single cone with the metal nanoparticles coated the cone. The resonance em field concentrates in close vicinity to the cone. Since the the shortest distance between the cones $d = 2.1 \mu\text{m}$ is significantly larger than the cone size (see Fig. 4) the inter-cone interaction can be neglected. Yet the collective interaction can be important for the mid-IR frequency band, where the wavelength $\lambda \simeq d$. We speculate that a collective surface mode can be excited in this case.

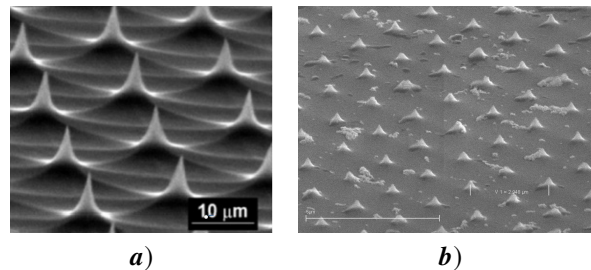


Fig. 1. Scanning electron image (SEM) of silicon tip-shaped metasurface; on right image it is possible to distinguish aggregates of gold nanoparticles that are deposited on metasurface.

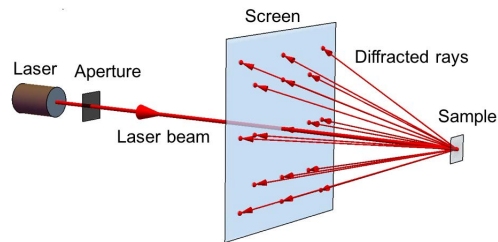


Fig. 2. Scheme of the laser beam passing through the circular hole in the screen, reflecting from the metasurface and making a diffraction pattern on the other side of the screen.

3. Electric and magnetic resonances in cone nanoparticles

The electric field enhancement in dielectric micro particles is a well known phenomenon. Electric and magnetic resonances can be excited in any particle made, for example, of silica, ceria and other dielectrics [19, 33, 52]. The electromagnetic (em) field enhancement in whispering gallery resonances is used in bio and chemical sensing [53] including detecting micro- and nanoparticles [54], virus [18] and, even, single molecule [2, 55]. The size of whispering gallery resonators is typically much larger than the wavelength. Yet, the electric field could be concentrated in a hot spot, which size is much smaller than the wavelength [23, 24].

Electromagnetic enhancement factor of SERS $G = \langle |\mathbf{E}_\omega(\mathbf{r})|^2 |\mathbf{E}_{\omega-\Delta\omega}(\mathbf{r})|^2 \rangle / |\mathbf{E}_0|^4$, where $\Delta\omega$ is the Stokes shift (see [26–28]), depends on the shape and arrangement of the resonators. It seems promising to use tip-shaped particles to concentrate a hot spots over the surface. Some properties of cone shaped metallic arrays were theoretically considered in [56].

Since the inter-cone spacing d is much larger than the wavelength in the visible frequency range, we focus on a single cone-shaped particle. We use the finite-difference frequency-domain (FDFD) method for numerical calculations in COMSOL Multiphysics environment. In the computer simulations the plane electromagnetic wave is incident from the vacuum on a single cone-shaped particle [Fig.4(a)]. The cone-shaped target is made of material with refractive index $n = 4$, which

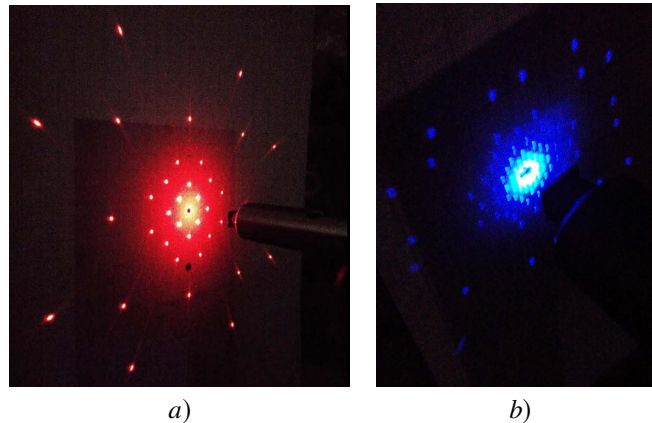


Fig. 3. Photos of the diffraction pattern produced by the metasurface from a normally incident polarized laser beam; a) laser power $I = 34.8 \text{ mW}$, wavelength $\lambda = 632.8 \text{ nm}$, the circular hole diameter 1.0 mm , the distance between screen and the metasurface is 20 mm ; b) blue laser beam, wavelength $\lambda = 405 \text{ nm}$.

approximates the silicon refractive index for $\lambda > 550 \text{ nm}$ [51]. The electric field distribution is computed for a wide frequency range, yet, we are focusing at visible and near infrared ranges due to the SERS application. The volume of the cone was chosen to be equivalent to the volume of the tip-shaped inclusions in the silicon metasurface we experimentally investigate. Figures 4(b)-5(i) present strong em resonances in the optical and IR frequencies. In the resonance the electric field is much enhanced with respect to the incident light. The silicon cone resonator exhibits various em modes including dipolar modes and hybrid whispering gallery modes (WGM) [Figs. 5(a)-6(h)]. At a large wavelength (resonances at wavelength $\lambda = 820, 790 \text{ nm}$) the field concentrates at the apex of the cone.

We develop a semi-quantitative analysis of em field oscillations, the resonance frequencies, and em field enhancement in a cone dielectric resonator. For this purpose it is convenient to introduce a spherical coordinate system, which has its origin in the cone vertex. That is the cone vertex has coordinates $x = y = z = 0$. The axis "z" originates from the vertex and coincides with the cone shaft as it is shown in Fig. 4(a). Inside the cone the polar angle $\theta < \theta_0$, where $2\theta_0$ is the cone opening angle. The permittivity of the surrounding space is equal to 1 and the harmonic time dependence $\sim \exp(-i\omega t)$ is assumed for all the em fields and currents. The axial symmetry of the cone results in angular momentum quantization and excitation of the modes with polar quantum number l , azimuthal quantum number m , and radial quantum number q . Various em resonances can be seen in Figs. 4 – 6 at closely spaced frequencies, corresponding to different polar and axial degrees of freedom. The highest quality factor $Q = \lambda/\Delta\lambda$ corresponds to WGM with minimal l and q but large m . The modes with small polar and radial "quantum" numbers propagate along the side surface of the cone. Besides the internal modes shown in Figs. 5(a)-5(i) and 6(a)-6(h), there are also external modes with much lower Q factor with em fields partially located outside the cone boundary. These modes correspond to the "leaky" region and can be explained in terms of the Husimi function, when the condition for the total internal reflection is violated $|\sin\chi| \leq 1/n$, where $\chi \approx \frac{\pi}{2}(1 - \frac{2}{m})$ is the angle of the "incidence" inside the cone (see [19]). In general the high Q modes in a dielectric resonator are typical for the small wavelength λ . For example, for silica microspheres the record $Q \approx 8 \times 10^9$ is achieved [11].

To estimate the resonance frequencies the vector potential $A^{(l,m)}$ for the em oscillations in the

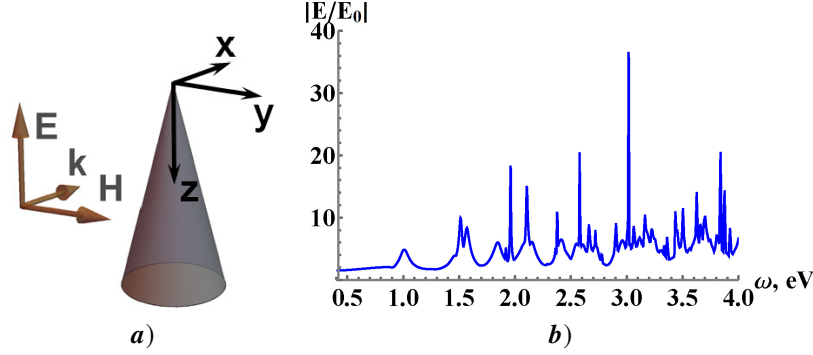


Fig. 4. a) Scattering from the cone dielectric resonator, direction \mathbf{k} of the incident light is perpendicular to the cone shaft; b) maximum of electric field $|E/E_0|$ inside the resonator as function of frequency of the incident light; the cone parameters are: vertex radius 10 nm , bottom radius 160 nm , height 595 nm , cone opening angle $2\theta_0 = 30^\circ$, refraction index $n = 4$; E_0 is amplitude of the incident light; calculation step $\Delta\lambda = 1\text{ nm}$.

dielectric cone resonator is taken in the standard form

$$\mathbf{A}^{(l,m)}(r, \theta, \varphi) = E_0 n \mathbf{r} \frac{J_{l+\frac{1}{2}}(r_1)}{\sqrt{r_1}} F_1(l, m, \theta) \sin^m \theta \begin{pmatrix} \cos m\varphi \\ \sin m\varphi \end{pmatrix}, \quad (1)$$

where E_0 is the electric field amplitude, defined by the incident em field, $\mathbf{r} = \{r, 0, 0\}$ is the radius vector, $r_1 = nkr$ is the dimensionless radius radiated from the cone vertex, n is the refraction index, the wave vector $k = \omega/c = 2\pi/\lambda$, the polar angle θ changes from zero to θ_0 inside the cone, the azimuth angle $0 \leq \varphi \leq 2\pi$, $J_{l+\frac{1}{2}}(r_1)$ is the Bessel function of the first kind, $F_1(l, m, \theta) = F(m-l, l+m+1; m+1; \sin^2 \frac{\theta}{2})$ is the Hypergeometric function, which is defined in a usual way, namely, $F(a, b; c; x) = \sum_{n=0}^{\infty} \frac{\Gamma(a+n)\Gamma(b+n)\Gamma(c)x^n}{[\Gamma(a)\Gamma(b)\Gamma(c+n)n!]}$. It is convenient to consider the em field in the narrow cone in terms of a Hypergeometric function since it has simple behavior for $\theta_0 \ll 1$: $F(m-l, l+m+1; m+1; \sin^2 \frac{\theta}{2}) \Rightarrow 1$, for $\theta \rightarrow 0$. For the integer l the function $F_1(l, m, \theta)$ is proportional to the usual Legendre polynomial $P_l^m(\cos \theta)$.

It is of common knowledge that there are “electric” and “magnetic” em modes in the cone resonator. The electromagnetic field for the “electric” oscillations equals to $\mathbf{H}_E^{(l,m)} = \text{curl } \mathbf{A}^{(l,m)}$, $\mathbf{E}_E^{(l,m)} = i \text{curl } \mathbf{H}_E^{(l,m)} / (n^2 k)$ and the field for the “magnetic” oscillations equals to $\mathbf{E}_M^{(l,m)} = \text{curl } \mathbf{A}^{(l,m)}$, $\mathbf{H}_M^{(l,m)} = -i \text{curl } \mathbf{E}_M^{(l,m)} / k$. For example, the magnetic field in the “electric” mode equals to: $H_{E,r}^{(l,m)} = 0$,

$$H_{E,\theta}^{(l,m)} = -E_0 m n \frac{J_{l+\frac{1}{2}}(r_1)}{\sqrt{r_1}} F_1(l, m, \theta) \sin^{m-1} \theta \begin{pmatrix} \sin m\varphi \\ \cos m\varphi \end{pmatrix}, \quad (2)$$

$$H_{E,\varphi}^{(l,m)} = E_0 n \frac{J_{l+\frac{1}{2}}(r_1)}{2(m+1)\sqrt{r_1}} F_3(l, m, \theta) \sin^{m-1} \theta \begin{pmatrix} \cos m\varphi \\ \sin m\varphi \end{pmatrix}, \quad (3)$$

and the components of the magnetic field in the “magnetic” mode equals to

$$H_{M,r}^{(l,m)} = -i E_0 n l (l+1) \frac{J_{l+\frac{1}{2}}(r_1)}{r_1} F_1(l, m, \theta) \sin^m \theta \begin{pmatrix} \cos m\varphi \\ \sin m\varphi \end{pmatrix}, \quad (4)$$

$$H_{M,\theta}^{(l,m)} = i E_0 n \frac{R(r_1)}{2(m+1)r_1^{3/2}} F_3(l, m, \theta) \sin^{m-1} \theta \begin{pmatrix} \cos m\varphi \\ \sin m\varphi \end{pmatrix}, \quad (5)$$

$$H_{M,\varphi}^{(l,m)} = i E_0 m n \frac{R(r_1)}{r_1^{3/2}} F_1(l, m, \theta) \sin^{m-1} \theta \begin{pmatrix} \sin m\varphi \\ \cos m\varphi \end{pmatrix}, \quad (6)$$

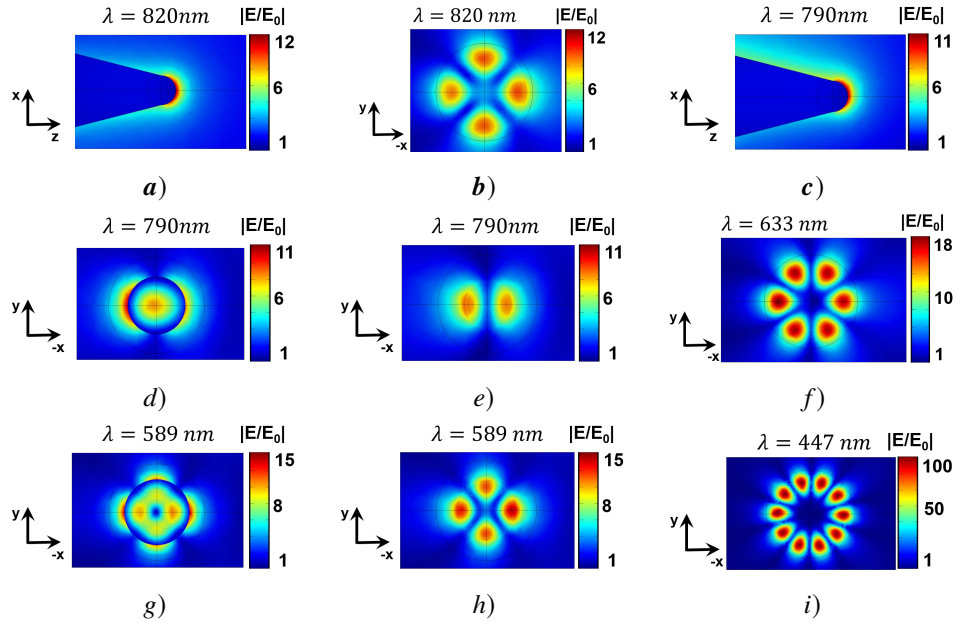


Fig. 5. Electric field distribution $|E(x, y, z)/E_0|$ for the resonance wavelengths in the dielectric cone resonator whose parameters are given in Fig. 4; light is incident normal to the cone shaft, electric field is aligned with the shaft (see Fig. 4); red color corresponds to the maximum amplitude of the electric field while the blue color corresponds to the minimum; the field is normalized to the amplitude of the incident field E_0 ; bottom of the cone is placed on plane $z = 0$; a) $\lambda = 820 \text{ nm}$, top of the cone; b) $\lambda = 820 \text{ nm}$, $m = 4$, cut plane $z = 80 \text{ nm}$; c) $\lambda = 790 \text{ nm}$, top of the cone; d) $\lambda = 790 \text{ nm}$, cut plane $z = 340 \text{ nm}$; e) $\lambda = 790 \text{ nm}$, cut plane $z = 250 \text{ nm}$; f) $\lambda = 633 \text{ nm}$, $m = 6$, cut plane $z = 80 \text{ nm}$; g) $\lambda = 589 \text{ nm}$, $m = 4$, cut plane $z = 190 \text{ nm}$; h) $\lambda = 589 \text{ nm}$, $m = 4$, cut plane $z = 260 \text{ nm}$; i) $\lambda = 447 \text{ nm}$, $m = 10$, cut plane $z = 80 \text{ nm}$.

where the dimensionless radius $r_1 = nkr$, $m = 1, 2, 3 \dots$; the function $F_1(l, m, \theta)$ is defined in Eq. (1); the functions $F_3(l, m, \theta)$ and $R(r_1)$ in Eqs. (3), (5) and (6) equal to

$$F_3(l, m, \theta) = (l - m)(l + m + 1)F_2(l, m, \theta) \sin^2 \theta - 2m(m + 1)F_1(l, m, \theta) \cos \theta, \quad (7)$$

$$R(r_1) = (l + 1)J_{l+\frac{1}{2}}(r_1) - r_1 J_{l+\frac{3}{2}}(r_1), \quad (8)$$

correspondingly; where the function $F_2(l, m, \theta)$ is also Hypergeometric function, namely, $F_2(l, m, \theta) = F(-l + m + 1, l + m + 2; m + 2; \sin^2 \frac{\theta}{2})$. In all these equations, the only "true" quantum number is the azimuthal number m , which is always integer due to the axial symmetry of a cone. The index l takes a positive value, which is defined from the boundary condition at the side surface of the cone $\theta = \theta_0$. Recall that $2\theta_0$ is the cone opening angle. Since l is a real value the azimuthal number m can take arbitrary large integer number. Therefore, it is easy to excite WGMs that "rotate" around the axis "z", i.e., the cone shaft. The em field in the large m modes has minimum at the cone shaft and em field concentrates near the cone surface $\theta \sim \theta_0$ as it follows from Eqs. (2)-(6) and can be seen in Figs. 5(a)-6(h), where we present results of our computer simulations and analytical, generic theory.

We consider, for simplicity, the case of the cone made of material with large refractive index $n \gg 1$. The magnetic field H in a em mode inside the resonator is proportional to $H \sim nE$ that is $H \gg E$ when $n \gg 1$ as it follows from the Maxwell equations. Outside the resonator the em field has the form of an evanescent wave, where $H \sim E$. Since the tangential components of the electric

and magnetic fields are continuous, their values inside the cone near the surface must be related in the same way. Therefore, the magnetic field at the cone surface is much smaller than the inside field. For the qualitative analysis we assume that the tangential component of the magnetic field approximately equals to zero at the surface of the cone. First we consider the “electric” mode [see Eqs. (2) and (3)]. Then the boundary condition at the side surface of the cone $H_{E,\varphi}(r, \theta_0, \varphi) = 0$ results in the equation $F_3(l, m, \theta_0) = 0$. We fix the “true” quantum number m . Then the roots $l_{E1}, l_{E2}, \dots, l_{Ep}, \dots$ of the equation $F_3(l, m, \theta_0) = 0$ give the parameter l . The boundary condition at the bottom surface of the narrow cone is $H_{E\theta}(h, \theta, \varphi) = H_{E\varphi}(h, \theta, \varphi) = 0$, where h is the cone height. The bottom boundary condition results in the equation $J_{l_{Ep} + \frac{1}{2}}[nkh = \nu_E(m, p, q)] = 0$, as it follows from Eqs. (2) and (3). The dimensionless resonance frequency $\nu_E(m, p, q)$ equals to the $q - th$ root ($q = 1, 2, 3, \dots$) of the Bessel function of the first kind of the order $l_{Ep} + \frac{1}{2}$. The dimensionless resonance frequency $\nu_M(m, p, q)$ of a “magnetic” em mode is obtained from the equations $H_{Mr}(r, \theta_0, \varphi) = H_{M\varphi}(r, \theta_0, \varphi) = 0$ and $H_{M\theta}(h, \theta, \varphi) = H_{M\varphi}(h, \theta, \varphi) = 0$ where θ_0 is the half of the cone opening angle and h is the cone height. Then Eqs. (4)-(6) give the equations $F_1(l_M, m, \theta_0) = 0$ and $R(\nu_M) = (l_M + 1)J_{l_M + \frac{1}{2}}(\nu_M) - \nu_M J_{l_M + \frac{3}{2}}(\nu_M) = 0$, where $\nu_M \equiv \nu_M(m, p, q)$ is the dimensionless “magnetic” resonance frequency. Thus obtained electric and magnetic dimensionless resonance frequencies ν_E and ν_M are defined by the cone geometry, namely, they depend on the cone opening angle $2\theta_0$ only. Real resonance frequencies are obtained from the equation $nkh = \nu_{E,M}$. We consider the cones with $2\theta_0 = 30^\circ$ that is $\theta_0 = \pi/12$. The lower dimensionless resonance frequencies of the $\theta_0 = \pi/12$ cone are

$$\nu_E(1, 1, 1) = 11.18, \nu_E(1, 1, 2) = 14.92, \nu_E(2, 1, 1) = 16.42, \quad (9)$$

$$\nu_M(0, 1, 1) = 11.05, \nu_M(0, 1, 2) = 15.55, \nu_M(1, 1, 1) = 16.78. \quad (10)$$

Note that the electric and magnetic resonances have almost the same frequencies when the azimuthal numbers m differ by one, i.e., $\nu_E(m + 1, p, q) \approx \nu_M(m, p, q)$. The doublet resonances can be clearly seen in Fig. 4(b) and Fig. 7. The em field distribution in the cone resonances is shown in Figs. 6(a)-6(h) for the lower frequencies given by Eqs. (9)-(10). We also show intensity of the electric field for the higher azimuthal numbers m when the analytical solution gives the resonance field in the form of WGM (see Figs. 6(g) and 6(h)). The resonance frequencies for the cone resonator, where the refraction index $n \gg 1$, is obtained from the equations $nkh = \nu_E$ or $nkh = \nu_M$, where h is the cone height; the frequencies equal to $\omega_{E,M}(m, p, q) = \frac{c}{nh} \nu_{E,M}(m, p, q)$. We use this equation to estimate the resonance frequencies for the cone with $n = 4$, $\theta_0 = \pi/12$, $h = 595 \text{ nm}$ obtaining the lower resonances

$$\omega_M(0, 1, 1) = 0.92 \text{ eV}, \omega_E(1, 1, 1) = 0.93 \text{ eV}, \omega_E(1, 1, 2) = 1.24 \text{ eV}, \quad (11)$$

$$\omega_M(0, 1, 2) = 1.29 \text{ eV}, \omega_E(0, 1, 1) = 1.63 \text{ eV}, \omega_E(0, 1, 2) = 1.98 \text{ eV} \quad (12)$$

that are similar to the resonances obtained in the computer simulations (see Fig. 5(b)). The spectrum of the resonance frequencies for the cone resonator is presented in Fig. 7. Electric and magnetic resonances are shown by red and blue colors correspondingly. The density of the resonances increases with increasing the frequency. The resonances are non-degenerate due to a low symmetry of the resonator. For the frequency greater than 3 eV the spectrum looks like quasi-continuum, it means that it is possible to find either electric or magnetic resonance in a vicinity of any given frequency.

The angular dependence of the em field in the cone is given by dimensionless Hypergeometric functions $F_1(l, m, \theta)$ and $F_2(l, m, \theta)$ that have a characteristic scale $\sim l + m$. To satisfy the boundary conditions at $\theta = \theta_0 \ll 1$ of a narrow cone the parameter l should be large, namely, $l \gtrsim \theta_0^{-1} \gg 1$. We expand the functions in series of $\sin \frac{\theta}{2}$ and take limit $l \rightarrow \infty$ in each term. We obtain, in the case when $l \gg 1$ and $l \gg m$, the function $\sin^m \theta F_1(l, m, \theta)$, which enters the equations for the

em field [see Eqs. (2)-(6)], is approximated as

$$\sin^m \theta F_1(l, m, \theta) = m! \left(\frac{2}{l} \cos \frac{\theta}{2} \right)^m J_m \left(2l \sin \frac{\theta}{2} \right), \quad (13)$$

where J_m is the Bessel function of the first kind of the order m . The same approximation holds for the function $F_2(l, m, \theta)$, but the index m should be replaced by $m + 1$. The Bessel approximation (13) allows to simplify the field calculation in the cone dielectric resonator.

To understand the em field behavior in the vicinity of the cone vertex we consider the simplest case, namely, the electric oscillations with azimuth number $m = 0$. In this case the magnetic field $H_E^{(l,0)} \equiv H^{(l)}$ has only azimuth component. We use the Bessel approximation (13) assuming that the cone opening angle $\theta < \theta_0 \ll 1$ and obtain

$$H_\varphi^{(l)}(r, \theta) = \theta l(l+1)nJ_1(l\theta)J_{l+\frac{1}{2}}(r_1)/2\sqrt{r_1} \quad (14)$$

the electric field equals to

$$E_r^{(l)}(r, \theta) = il(l+1)J_0(l\theta)J_{l+\frac{1}{2}}(r_1)/r_1^{3/2} \quad (15)$$

$$E_\theta^{(l)}(r, \theta) = -i\theta l(l+1)J_1(l\theta)R(r_1)/2r_1^{3/2} \quad (16)$$

where $r_1 = nkr$; the functions J_0 , J_1 , and $J_{l+\frac{1}{2}}$ are the Bessel functions of the first kind; the function $R(r_1)$ is defined by Eq. (8). To further simplify the consideration we suppose that the refraction index $n \gg 1$. Then the boundary condition at the side face of the cone [$H_\varphi^{(l)}(r, \theta_0) \approx 0$] gives the index $l_p = \mu_p/\theta_0$, where μ_p is the p^{th} root of zero Bessel function: $J_1(\mu_p) = 0$, e.g., $\mu_1 = 3.83$ and $l_1 = \mu_1/\theta_0 = 14.64$ for the considered cone, where $\theta_0 = \pi/12$. We obtain that $l_1 \gg 1$ and the Bessel approximation (13) holds indeed. The boundary conditions at the bottom face of the cone is $H_\varphi^{(l)}(h, \theta_0) \approx 0$. It gives the dimensionless resonance frequency $nkh = \nu(p, q)$, where h is the cone height and $\nu(p, q)$ is the q^{th} root of the l_p^{th} Bessel function: $J_{l_p+\frac{1}{2}}(\mu_q) = 0$. For the considered cone with $n = 4$, $\theta_0 = \pi/12$, and $h = 595 \text{ nm}$ [see Figs. 4(a)-6(h)] the first two frequencies are estimated as $\omega_E(0, 1, 1) = 1.62 \text{ eV}$ and $\omega_E(0, 1, 2) = 1.98 \text{ eV}$. These results coincide with “exact” Eq. (12).

It follows from Eqs. (15) and (16), that electric field vanishes as $|E(r)|^2 \sim \frac{e^3}{64\pi} [\theta^2 l_p^2 J_1(l_p \theta)^2 + 4J_0(l_p \theta)^2] \left(\frac{er_1}{2l_p} \right)^{2(l_p-1)}$ when $r \rightarrow 0$ (recall $r_1 = nkr$). Therefore, em modes, excited in the cone, do not reach the vertex from within. To estimate the electric field at the top of the cone, where the local radius $\rho_r = r \tan \theta_0$ is small enough so that $\rho nk < 1$ we use the quasistatic approximation, which is in detail explained in our recent work [24]. We obtain the following estimate $|E_s|^2 = n^4 |\mathbf{E}_z \cdot \mathbf{s}|^2 + |\mathbf{E}_z \times \mathbf{s}|^2$, for the electric field intensity at the outer surface of the cone, where \mathbf{E}_z is a component of the external field aligned with the cone shaft, \mathbf{s} is the unit vector perpendicular to the cone surface. This result holds for a narrow cone with small opening angle $\theta_0 \ll 1$. There is always natural regularization of the vertex singularity in the cone resonator. The vertex of the dielectric cone always has a finite radius ρ of the curvature. Thus we obtain two orders on magnitude enhancement of the local electric field intensity at the vertex of the silicon cone whose the refractive index $n \approx 4$. The field enhancement at the top of the cone resonator is clearly seen in Figs. 5(a)-5(d). We also speculate that the external field \mathbf{E}_z could be much enhanced as compared with incident em wave in the case of the resonating cone.

4. Metal-dielectric resonances

A standard procedure to reach large enhancement of local electric fields is duly arrange gold (Au) or silver (Ag) nanoparticles in plasmon resonators. The resonant nature of metal nanoparticles in

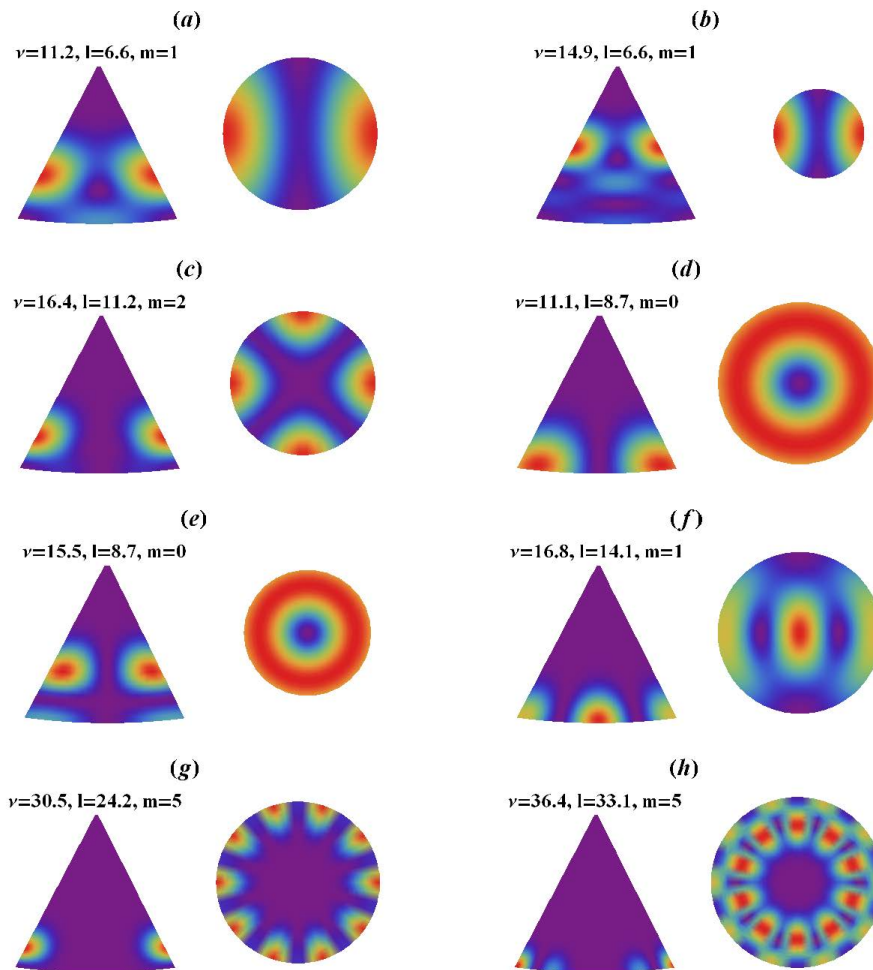


Fig. 6. Electric field intensity $|E(r, \theta, \phi)|^2$ in dielectric cone resonator with opening angle 30° and refractive index $n \gg 1$; "electric" resonances are shown in Figs. 7(a),(b),(c) and (g); "magnetic" resonances are shown in Figs. 7(d),(e),(f) and (h); each resonance is labeled by dimensionless frequency $\nu = nkh$, orbital number l and azimuthal number m ; the low symmetry of the resonator results in noninteger orbital number l .

optics has been studied in numerous works starting from seminal work of Michael Faraday's (for recent references see, e.g., [57–59]). The electric field E in a sub-wavelength spherical metal nanoparticle can be estimated as $E_{in} \approx E_0/(\epsilon_m + 2\epsilon_d)$, where ϵ_m and ϵ_d are permittivities of the metal and the surrounding space correspondingly. According to [60] the plasmon resonance of an isolated Au nanoparticle is excited in the air at $\lambda \approx 500 \text{ nm}$. We consider a metal-dielectric resonator, which is a spherical gold particle with the radius a surrounded by the spherical dielectric envelope with the thickness Δ as it is shown in Fig. 8(a). Such a spherical sandwich structure was considered previously using the hybridization approach (see e.g. [61, 62] and references therein). The refractive index of the dielectric layer equals to $n = 2.5$, which approximately corresponds to the average refraction of air and silicon; the refraction index of an ambient medium is assumed to be one. The result of computer simulations of the light scattering by a metal-dielectric resonator



Fig. 7. Spectrum of em resonances in cone resonator; cone opening angle 30° , refraction index $n = 4$, height $h = 595 \text{ nm}$; frequencies of electric and magnetic resonances are shown by red and blue lines correspondingly.

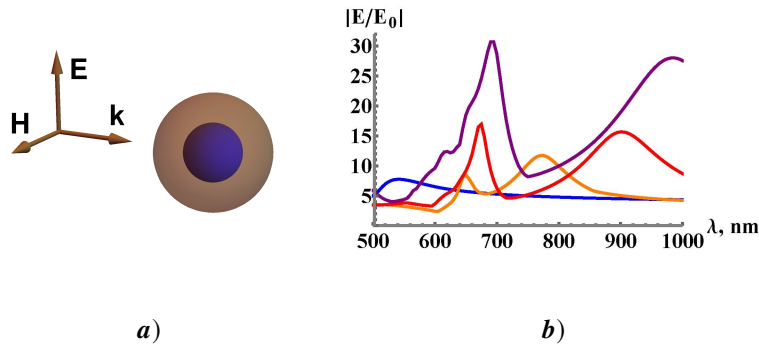


Fig. 8. a) Metal-dielectric spherical resonator (Russian doll); b) Electric field enhancement $|E_{max}/E_0|$ in the resonator gold core for different thickness Δ of dielectric layer; the parameters are: radius of gold particle $a = 50 \text{ nm}$, refractive index of dielectric layer $n = 2.5$; blue line corresponds to isolated Au particle without dielectric layer; orange line for thickness of dielectric layer $\Delta = 50 \text{ nm}$, red line for $\Delta = 100 \text{ nm}$, purple line for $\Delta = 150 \text{ nm}$.

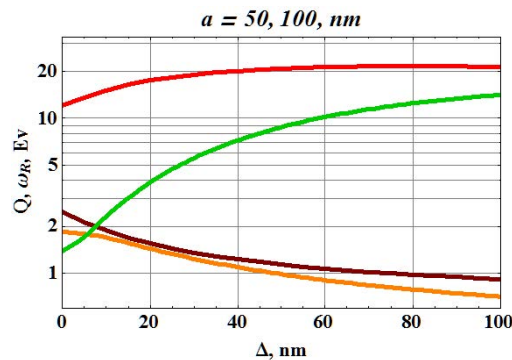


Fig. 9. Resonance frequency ω_R (drop-down curves) and quality factor Q (up-going curves) of gold-dielectric resonator, shown in Fig. 8, as function of thickness Δ of dielectric layer, refraction index $n = 4$; brown and red curves correspond to gold core radius $a = 50 \text{ nm}$, orange and green to $a = 100 \text{ nm}$

composed of Au nanoparticle, placed in the dielectric case, is shown in Fig. 8(b). When the thickness Δ of the dielectric layer is larger than the radius of Au nanoparticle ($\Delta > a$), the resonance frequency of the metal-dielectric resonator become closer to the dipolar resonance of the dielectric sphere of the radius $b = a + \Delta$. For example, according to the asymptotic solution of Eq. (7) in our paper [23], the resonance of the dielectric sphere with the radius $a = 200 \text{ nm}$ and the refraction index $n = 2.5$ corresponds to $\lambda = 690 \text{ nm}$, which is in agreement with Fig. 8(b). The existence of the dielectric layer provides a shift in the plasmon resonance of an isolated metal particle and the electric field is increased due to the generation of plasmon-dielectric resonance.

The effect of a cascade field enhancement in hybrid optoplasmonic structures was studied in works [23, 37, 38, 63, 64]. Hybrid photonic-plasmonic modes are already used in WGM resonators to detect standard Bovine Cerium Albumin protein [65].

We believe that the increase of the quality factor Q in metal-dielectric resonators is due to the decrease of the radiation loss. The conducting current in the metal part of the resonator and the polarization current, excited in the dielectric, flow in the opposite directions since the metal permittivity is mainly negative. The radiation loss is proportional to the sum of currents and, therefore, the loss decreases in a resonator, where permittivity is of different signs.

To quantitatively discuss the dielectric screening we consider the eigenstate of a plasmonic nanoparticle of radius a surrounded by a spherical dielectric envelope with radius $b = a + \Delta > a$, where Δ is thickness of the dielectric layer. We consider, for simplicity, the electric dipole eigenstate. Then, the electric field outside the metal-dielectric resonator is given by magnetic vector potential

$$\mathbf{A}_e = i\mathbf{n}_z E_0 b e^{ik(r-b)} / (kr), \quad (17)$$

where \mathbf{n}_z is the unite vector in z direction. The outside magnetic and electric fields equal to $\mathbf{H}_e = \text{curl } \mathbf{A}_e$ and $\mathbf{E}_e = -i\text{curl } \mathbf{H}_e / k$ for $r > b$. The magnetic field \mathbf{H}_e rotates around the z axis. It is still convenient to use the spherical coordinates r, θ, φ . Then the magnetic field \mathbf{H}_e has the component H_φ only. The coefficient for the external vector potential \mathbf{A}_e in Eq. (17) is chosen to meet the radiation boundary conditions at infinity $E_e \rightarrow (b/r)E_0 e^{ik(r-b)} \sin \theta$ for $r \rightarrow \infty$.

In the dielectric layer (see Fig. 8), for the radius $a < r < b$ the em field is given by the vector potential

$$\mathbf{A}_f = ia \left[A e^{ikn(r-a)} + B e^{-ikn(r-a)} \right] / kr, \quad (18)$$

which is composed of the inward and backward spherical waves. That is the dielectric layer reflects the em field radiating from the metal core. The coefficients A and B are chosen to fit the boundary conditions $E_{e,\theta}(r=b) = E_{f,\theta}(r=b)$, $H_{e,\varphi}(r=b) = H_{f,\varphi}(r=b)$ at the outer boundary of the metal-dielectric resonator. The field inside the metal nanoparticle is given by the vector potential $\mathbf{A}_i = -3iE_{in} \sinh(r_1) / (2kr_1)$, where it is convenient to denote $r_1 = kr\sqrt{-\varepsilon_m} \sim (\omega_p/c)r$, where c/ω_p is the skin depth in Drude approximation; the electric field E_{in} is the field in the center of the metal core of the metal-dielectric resonator. The value of the “central” electric field E_{in} is obtained from the field-matching at the metal-dielectric interface $E_{i,\theta}(r=a) = E_{f,\theta}(r=a)$. The second boundary condition $H_{i,\varphi}(r=a) = H_{f,\varphi}(r=a)$ gives the dispersion equation for the eigenfrequency $\omega = \omega_1 + i\omega_2$, which is complex due to the radiation loss. We chose the radiating boundary equation in Eq. (17), hence, the imaginary part of the eigenfrequency is negative $\omega_2 < 0$. The quality factor of the resonator $Q = -\omega_1 / (2\omega_2)$ defines the em field enhancement in the resonance.

We consider the plasmon resonance in the gold nanoparticle of the radius a , which corresponds to our experimental situation. For a rough estimate we use the Drude approximation $\varepsilon_m = \varepsilon_b - (\omega_p/\omega)^2 / (1 + \omega_\tau/\omega)$, where the parameters of $\varepsilon_b = 4.1$, $\omega_p = 8.7$ eV, $\omega_\tau = 0.11$ eV are chosen to fit the experiment [60] for $\omega < 2$ eV. The quality factor of the naked gold particles with size of $a_1 = 50$ nm and $a_2 = 100$ nm equals to $Q_1 \approx 12$ and $Q_2 \approx 1.4$ correspondingly. The drop of the resonance quality Q by an order on magnitude with doubling the radius is due to the radiation loss. It is not surprising since the radiation is proportional to $(ka)^3$. The Q factor increase when the metal nanoparticle is surrounded by the dielectric sphere, as it is shown in Fig. 9. We speculate that the increase of Q is due to the radiation screening by the dielectric layer.

We put the gold nanoparticle in the hot spot generated by the cone dielectric resonator (see the previous section). We focus on the resonance at wavelength $\lambda = 790$ nm, when the em field concentrates outside the cone. The local electric field $|E/E_0|$ in the metal-dielectric resonator of the gold nanoparticle and silicone cone reaches giant values that are more than two orders on magnitude larger then the amplitude of the incident field and the local SERS factor G can

be as large as 10^9 [Fig. 10(a)]. For double particle (two touchable spherical particles) factor G can be even larger 10^{11} [Fig. 10(b)]. Therefore, the conglomerate of gold particles could provide a stronger resonant behaviour into red and near infrared spectral range due to the excitation of multiple plasmon-dielectric resonances.

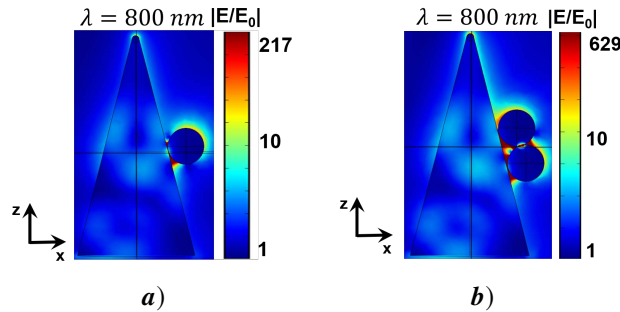


Fig. 10. a) Electric field distribution $|E(z, x)/E_0|$ for a gold particle with radius $a = 50 \text{ nm}$ placed on the surface of silicone cone; resonant wavelength $\lambda = 800 \text{ nm}$. b) Electric field distribution $|E(z, x)/E_0|$ for two gold particles (with equal radius $a_1 = a_2 = 50 \text{ nm}$) placed on the surface of silicone cone; resonant wavelength $\lambda = 800 \text{ nm}$; the field is applied along z axis, i.e., cone shaft; for cone parameters see Fig. 4.

5. SERS in metasurface

5.1. SERS tag preparation

The silicon tip metasurface, shown in Fig. 1(a), was modified by SERS-active tags, namely the gold nanoparticles (Au -NPs) with average size $55 \pm 5 \text{ nm}$ covered by semicontinuous monolayer of 5,5-dithio-bis(2-nitrobenzoic acid) (DTNB) molecules. The DTNB molecule use their sulfate groups to form chemical bonds with the gold nanoparticle [Figs. 11(a) and 11(b)] [31]. We measure the Raman signal from Au -NP to estimate the enhancement of the local electric field. The covered Au -NPs are not mere convenient indicators, they could interact with the cone resonators to form metal-dielectric resonances shown in Figs. 10(a) and 10(b). Au -NP were prepared by a well-known citrate method [66]. The conjugate of Au -NP-DTNB was adsorbed onto the cone metasurface after deposition of polycation film (polydiallyldimethylammonium chloride) according to the procedure described in [67].

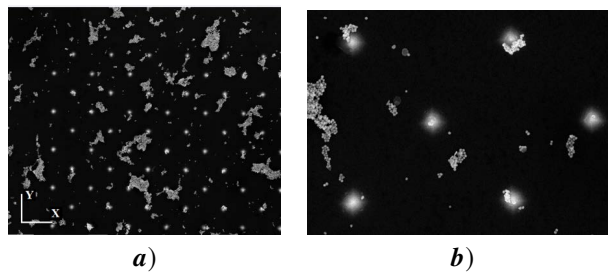


Fig. 11. SEM images in two scales of gold nanoparticles deposited on the silicon metasurface; bright blurred points, organized in regular lattice, are the apices of cone resonators (cf. Fig. 1).

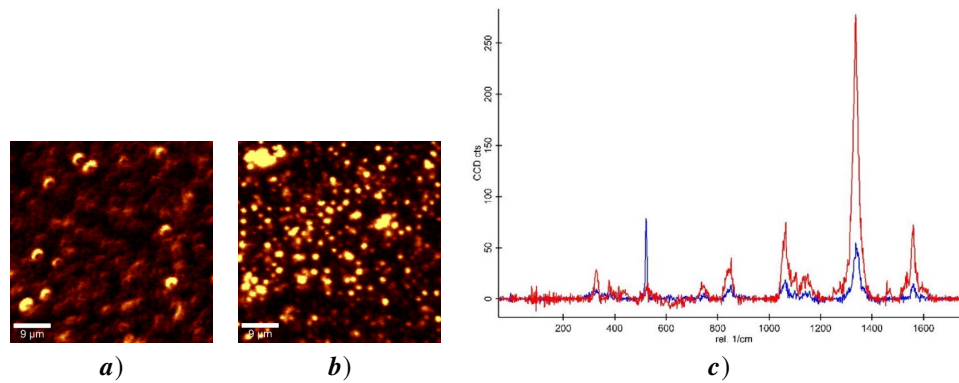


Fig. 12. Optical mapping of the intensity distribution for DTNB Raman spectral line with Stokes shift 1338 cm^{-1} a) Raman signal from the flat silicon film, b) Raman signal from the cone metasurface; the parameters of mapping are: 100x objective, mapping area $50 \times 50\ \mu^2$, step of scanning $\approx 0.56\ \mu$, depth of focus $\sim 0.5\ \mu$; c) intensity of Raman signal from *Au*-NP-DTNB as function of Stokes shift; blue color corresponds to the flat silicone region, red color corresponds to the cone metasurface.

5.2. Raman signal

We perform the experiment in two stages. Firstly SEM mapping is done, secondly, the Raman signal is measured. At first stage SEM image is performed with particular coordinate grid of metasurface. The fraction p of the surface occupied by the gold nanoparticles, is estimated from the SEM images by using GNU "Gwyddion" software. The surface fraction p of nanoparticles is estimated as 6.8% for the flat region, and 7.2% for the cone metasurface. The conjugate of *Au*-NP with DTNB (*Au*-NP-DTNB) has series of well defined Raman spectral lines and can be used as an effective SERS indicator. We use the Raman spectrometer of WITec Instruments Inc. to collect the spectra which are excited by the laser with the wavelength of 785 nm . The Raman spectrum is collected with 100x objective (NA=0.9). The Raman scattering of NO_2 line of DTNB with the Stokes shift 1398 cm^{-1} is used to investigate the SERS phenomenon.

The optical mapping of the intensity distribution for the Raman line 1338 cm^{-1} of DTNB is shown in Figs.12(a)-12(c). The result of the optical mapping was compared to the coordinate grid in SEM to find the signal from each point of the surface. We demonstrate a significant enhancement of the intensity distribution in the metasurface (red line) with respect to flat region (blue line). It can be explained by excitation of the metal-dielectric resonances in *Au*-NPs and silicone cones in the metasurface. The cone-shaped silicon tips operate as a resonators that convert the laser light into longitudinal electric field as we discussed in our recent paper [24]. The detailed research of spectra after the normalization to the amount of *Au*-NP shows that SERS signal depends on *Au*-NPs position at the surface. For example, Figs. 13-15 show the position of *Au*-NPs at the surface and Raman signal from each point of the surface. The signal after the normalization to the amount of *Au* nanoparticles is presented in Table 1. We are focusing on three characteristic points: 1) the conglomerate of *Au*-NP-DTNB on the flat silicone surface outside the cone metasurface [Fig. 13], 2) *Au*-NP-DTNB at the side surface of the silicone cone [Fig. 14], 3) the conglomerate of *Au*-NP-DTNB is the point equidistant between the cones [Fig. 15]. It can be seen from Table 1 that the intensity of Raman signal is two orders on magnitude larger for the tip-shaped metasurface than for the flat silicon film (outside the cone metasurface). The Raman signal enhancement is reached by placing *Au*-NP on the side face of a cone of the metasurface, where hot spots can exist (see Figs.10(a)-10(b) in the previous section). Therefore our theoretical prediction is confirmed. The results of the analytical theory and numerical calculations are in a

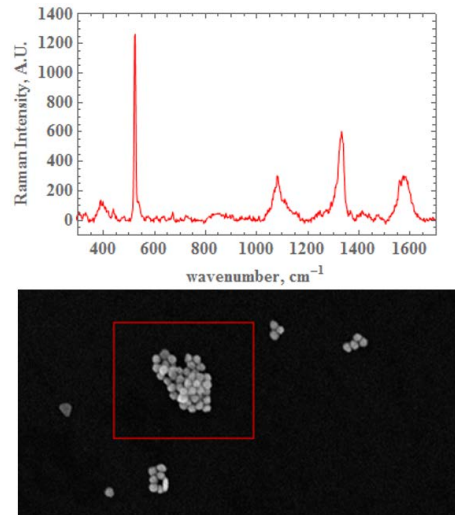


Fig. 13. Raman signal (from red frame) and SEM image of *Au*-NP-DTNB deposited on the flat silicone film out of grating.

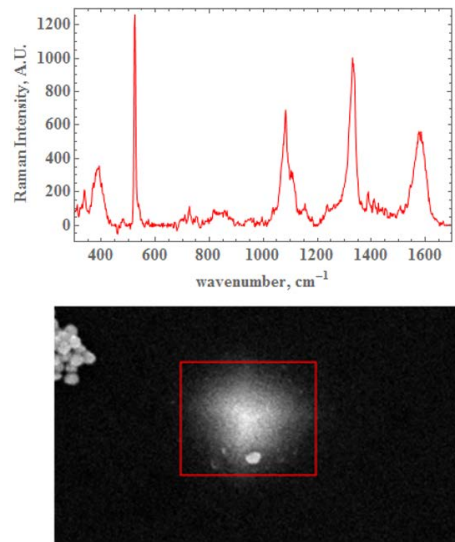


Fig. 14. Raman signal from *Au*-NP-DTNB placed close to silicon cone (bright blurred area).

qualitative agreement with our experimental results.

6. Conclusions

We investigate optical properties of the dielectric metasurface composed of silicon micro-tips. Our computer simulations reveal electric and magnetic resonances in the silicon cones. The resonances in the micro-cones result in a very bright diffraction. We develop the theory of em resonances in a cone dielectric resonator and find the spectrum of resonances. The hybrid metal-dielectric resonances are excited when metal nanoparticles are deposited on the surface of the silicon cones. When gold nanoparticles are placed in a proper place of the cone surface, the resonance electric field enhancement can be more than three orders on magnitude. Hence, the

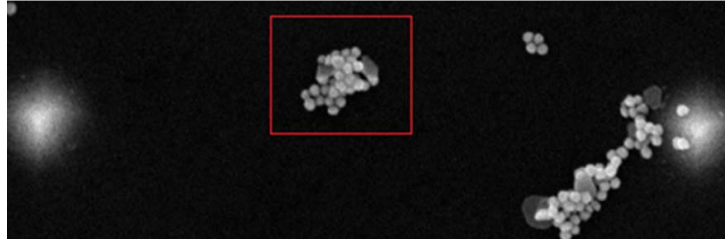
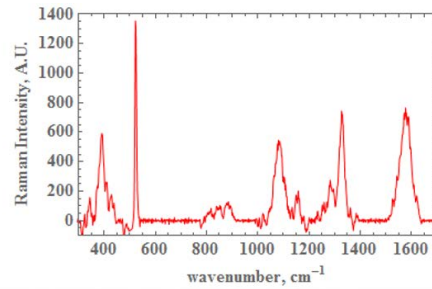


Fig. 15. Raman signal from *Au*-NP-DTNB placed in equidistant point between cones of the metasurface; signal collected from red frame.

Table 1. Intensity of Raman signal (Stokes shift 1338 cm^{-1}) from conjugate *Au*-NP-DTNB on the metasurface vs flat plane, a.u. (normalized to the amount of gold nanoparticles)

	Signal, CCD cts	Number of <i>Au</i> -NP	Normalized signal
The side of pyramid	786	1	786
Between pyramids	553	30	18.4
Out of grating	553	89	6.2

SERS, which is proportional to the fourth power, could be huge for the metal-dielectric resonance. We cover the surface of the gold nanoparticles with signal molecules and observe clear SERS from the metasurface. We can tune the frequency of the resonances by varying the cone height and opening angle. We can make the spectrum to fit the Raman spectrum of the substance we are interested in. The light localization in the dielectric resonator metasurface open new venue in R&D SERS substrates including sensors for determining the specific substances.

Funding

Russian Foundation for Basic Research (RFBR) (17-08-01448A).

Acknowledgments

Authors acknowledge very important discussions with V.I. Fabelinskii, D.N. Kozlov and G. Arzumaryan. Experimental samples were made at the BMSTU Nanofabrication Facility (Functional Micro/Nanosystems, FMNS REC).